Dynamic Analysis of Uniformity and Difference for Grid-following and Grid-forming Voltage Source Converters Using Phasor and Topological Homology Methods

Haiyu Zhao, *Member*, *IEEE*, Hongyu Zhou, *Member*, *IEEE*, Wei Yao, *Senior Member*, *IEEE*, Qihang Zong, *Member*, *IEEE*, and Jinyu Wen, *Member*, *IEEE*

***Abstract*—Grid-following voltage source converter (GFL-VSC) and grid-forming voltage source converter (GFM-VSC) have different dynamic characteristics for active power-frequency and reactive power-voltage supports of the power grid. This paper aims to clarify and recognize the difference between grid-following (GFL) and grid-forming (GFM) frequency-voltage support more intuitively and clearly. Firstly, the phasor model considering circuit constraints is established based on the port circuit equations of the converter. It is revealed that the voltage and active power linearly correspond to the horizontal and vertical axes in the phasor space referenced to the grid voltage phasor. Secondly, based on topological homology, GFL and GFM controls are transformed and mapped into different trajectories. The topological similarity of the characteristic curves for GFL and GFM controls is the essential cause of their uniformity. Based on the above model, it is indicated that GFL-VSC and GFM-VSC possess uniformity with regard to active power response, type of coupling, and phasor trajectory. They differ in synchronization, power coupling mechanisms, dynamics, and active power-voltage operation domain in the quasi-steady state. Case studies are undertaken on GFL-VSC and GFM-VSC integrated into a four-machine two-area system. Simulation results verify that the dynamic uniformity and difference of GFL-VSC and GFM-VSC are intuitively and comprehensively revealed.**

***Index Terms*—Renewable energy, grid-following converter, grid-forming converter, phasor method, topological homology.**

I. Introduction

POWER electronic converters for integrating renewable energy sources into power systems can be categorized into grid-forming (GFM) and grid-following (GFL) converters [1]. At present, converters widely used in real projects are usually voltage source converters (VSCs), which utilize a GFL control structure [2]. This control structure utilizes phase-locked loop (PLL) technique to synchronize with the power grid, which achieves power output or voltage regulation by controlling the injected current. However, the increasing penetration of renewable energy sources can lead to a weak grid at the receiving end. Grid-following voltage source converter (GFL-VSC) poses a risk of instability in weak grids. Therefore, in order to ensure the stable operation of the power system in weak grids, the VSCs need to be controlled as voltage sources instead of current sources. Currently, scholars refer the VSC controlled converter to be a voltage source as the grid-forming voltage source converter (GFM-VSC) [3]. Besides being controlled as a voltage source, GFM-VSC is also synchronized with the grid by controlling the power output. There are significant differences in the external characteristics and synchronization of GFL-VSC and GFM-VSC, which determine the characteristics of the grid-connected renewable energy [4]. These further result in different dynamic characteristics of GFL-VSC and GFM-VSC in terms of active power-frequency and reactive power-voltage supports [5]. The different frequency-voltage characteristics of these converters not only bring flexibility to the operation of the power systems, but also result in new control dynamics and instability problems [6].

GFL-VSC and GFM-VSC have their own advantages, disadvantages, and applicability in frequency-voltage support, which will have a profound impact on the renewable power system. It is of essential significance to clarify the difference between the frequency-voltage dynamics of GFL-VSC and GFM-VSC for planning the ratio of GFL-VSC and GFM-VSC in the power system and precisely controlling GFL-VSC and GFM-VSC in the operation process [7]. Existing studies have begun to conduct and discuss the difference between GFL-VSC and GFM-VSC from various perspectives. Some research works try to find uniformity to reveal the relationship between GFM-VSC and GFL-VSC. References [8] and [9] obtain the differences of GFL-VSC and GFM-VSC under strong and weak small-signal grid adaptation.

Manuscript received: July 7, 2024; revised: October 2, 2024; accepted: December 22, 2024. Date of CrossCheck: December 22, 2024. Date of online publication: January 30, 2025.

This work was supported by National Key R&D Program of China (No. 2022YFB4202304).

H. Zhao, H. Zhou, W. Yao (corresponding author), Q. Zong, and J. Wen are with State Key Laboratory of Advanced Electromagnetic Technology, School of Electrical and Electronics Engineering, Huazhong University of Science and Technology, Wuhan 430074, China (e-mail: zhaohaiyu2021@163.com; ee.henry_zhou@foxmail.com; w.yao@hust.edu.cn; qh_zong@hust.edu.cn; jinyu.wen@hust.edu.cn)

DOI: 10.35833/MPCE.2024.000722

The analysis of dynamic processes of GFL and GFM controls is not addressed [10]. References [11] and [12] provide the comparative analysis in terms of the control equations of converters, but they cannot intuitively reveal the frequency-voltage dynamics in the operation process intuitively. In [13], an analytical comparison of the active power response of GFL and GFM frequency-voltage controls is conducted using the transfer function. However, the derivation of the transfer function ignores the electrical constraints in actual operation and can only be analyzed in quasi-steady state. Reference [14] combines the advantages of the above methods and analyses the dual uniformity of GFL-VSC and GFM-VSC in a more comprehensive way.

In summary, the existing research works mainly focus on the static perspective and are conducted separately for both converters. Unfortunately, many ambiguities still exist regarding the participation of GFL-VSC and GFM-VSC in frequency and voltage dynamic support, which limits their frequency and voltage support capabilities [15], [16]. The ambiguities mainly include the following four aspects: ① differences in the dynamic characteristics of frequency and voltage regulation between GFM-VSC and GFL-VSC; ② the power coupling problem and the nature of the mechanism in frequency and voltage regulation between GFL-VSC and GFM-VSC; ③ whether the frequency and voltage support strategies of GFL-VSC can be transplanted to GFM-VSC and whether there is any unity between them; ④ whether there are similarities and differences between the frequency and voltage operation feasible domains of GFL-VSC and GFM-VSC.

To summarize and clarify the dynamic characteristics of GFL-VSC and GFM-VSC in terms of frequency and voltage support, the phasor method allows for a visualization of the relationships among the circuit variables after the converter is connected. Therefore, the phasor method has the potential to reveal the frequency-voltage relationship between GFL-VSC and GFM-VSC. Reference [17] introduces the method of using equivalent phasors to judge the current and voltage response processes of GFL-VSC and GFM-VSC. The effective combination of phasor and control makes the analysis more intuitive and clear. However, it only considers the phasor dynamics of the converter and does not consider the control dynamics of the converters. Reference [18] analyzes the transient voltage support process of the virtual synchronous generator by further using the phasor method and designs a fault ride-through scheme that considers the dynamic process. But it has not yet focused on the dynamic process of frequency-voltage support. In summary, the phasor method can provide a new scheme for characterizing the frequency-voltage relationship between GFL-VSC and GFM-VSC in a deterministic state. However, there are still challenges in revealing the dynamic change characteristics.

Recognizing GFL-VSC and GFM-VSC from the perspective of control dynamics will show the dynamic process of frequency-voltage support more intuitively compared with the existing methods [17]. Topological homology theory is a reliable one that mathematically characterizes the transformation relationship between different topologies. The theory can reveal the operation characteristics of GFL-VSC and GFM-VSC in various states through the perspective of topological transformations [19]. This provides the possibility to analyze the dynamic processes of GFL-VSC and GFM-VSC in multiple continuous states [20]. Therefore, this paper combines the advantages of the phasor method in describing the frequency-voltage relationship with the advantages of the topological homology theory in characterizing continuous topological dynamic changes, which focuses on identifying and clarifying the difference in GFL and GFM frequency-voltage support dynamics. Their uniformity and difference are investigated through theoretical derivation combined with simulation experiments.

In this paper, the dynamic uniformity and difference of GFL-VSC and GFM-VSC are analyzed using phasor and topological homology methods. The main contributions of this paper are as follows.

1) Phasor model is developed to reveal operation characteristics of GFL-VSC and GFM-VSC in terms of active power-frequency and reactive power-voltage. It is found that the operation points of GFL-VSC and GFM-VSC can be combined with frequency and voltage in the phasor space. The horizontal coordinate of the operation point is linearly proportional to the grid-connected voltage amplitude, and the vertical coordinate of the operation point is linearly proportional to the active power output.

2) The effects of GFL and GFM control dynamics and their coupling mechanisms are considered from a topological perspective. The topological homology theory is used to transform the controls into different trajectories in the phasor model. Thus, the dynamics of GFL-VSC and GFM-VSC can be portrayed by changes in topological trajectories.

3) The dynamic uniformity of GFL-VSC and GFM-VSC is reflected in active power response, type of coupling, and phasor trajectory. The dynamic difference of GFL-VSC and GFM-VSC is reflected in synchronization, power coupling mechanisms, dynamics, and active power-voltage operation domain in the quasi-steady state.

The rest of the paper is organized as follows. Section II introduces the analysis of key influences on the control dynamics of GFL-VSC and GFM-VSC using the phasor method. Section III presents the analysis of dynamic frequency-voltage uniformity and difference using topological homology theory. Section IV provides simulation results of the dynamic process. Section V presents the conclusions of this paper.

II. Analysis of Key Influences on GFL and GFM Control Dynamics Based on Phasor Method

A. Circuit Equivalent of GFL-VSC and GFM-VSC

As shown in Fig. 1, GFL-VSC requires PLL to synchronize with the external grid by making the phase angle follow the voltage sampling result at the point of common coupling (PCC) [21]. The mathematical model of GFL control is established as:

$$\begin{cases} \dfrac{\mathrm{d}\theta_{GFL}}{\mathrm{d}t} = \omega_{GFL} = k_{pPLL}U_{gq} + k_{iPLL}\displaystyle\int U_{gq}\mathrm{d}t \\ i_{dref,GFL} = k_{p1}(P_{sref} - P_s) + k_{i1}\displaystyle\int (P_{sref} - P_s)\mathrm{d}t \\ i_{qref,GFL} = k_{p2}(Q_{sref} - Q_s) + k_{i2}\displaystyle\int (Q_{sref} - Q_s)\mathrm{d}t \end{cases} \tag{1}$$

where θ_{GFL} is the synchronization angle of the PLL output for GFL-VSC; ω_{GFL} is the angular velocity of the PLL output for GFL-VSC; P_{sref} and Q_{sref} are the reference values of active power and reactive power from the converter, respectively; P_s and Q_s are the actual values of active power and reactive power from the converter, respectively; U_{gd} and U_{gq} are the *d*- and *q*-axis components of the voltage at the PCC, respectively; $i_{dref,GFL}$ and $i_{qref,GFL}$ are the *d*- and *q*-axis reference values of the output current of the converter, respectively; k_{pPLL} and k_{iPLL} are the proportional and integral coefficients of the PLL control, respectively; k_{p1} and k_{i1} are the proportional and integral coefficients for constant active power control, respectively; and k_{p2} and k_{i2} are the proportional and integral coefficients for constant reactive power control, respectively.

In Fig. 1, v_{abc} and i_{abc} are the grid-connected three-phase voltage and current, respectively; i_{dq} is the grid-connected current of *dq*-axis; I_s is the output current amplitude of the converter; Z_g is the total equivalent impedance of the grid; i_{dqref} is the *d*-*q*-axis reference values of the current in the inner-loop current control of the converter; U_g is the grid-side voltage magnitude; and U_{GFL} and U_{GFM} are the grid-connected voltage amplitudes of GFL-VSC and GFM-VSC, respectively. GFL-VSC achieves reactive power tracking by controlling the *q*-axis current to follow the reference value of reactive power. GFL-VSC also achieves active power tracking by controlling the *d*-axis current to track the reference value of active power. GFL-VSC is controlled as active power and reactive power source. The dual equivalent circuits of GFM-VSC and GFL-VSC are shown in Fig. SA1 of Supplementary Material A.

Unlike GFL-VSC, θ_{GFM} is the synchronization angle of GFM-VSC. GFM-VSC usually uses virtual synchronous control to achieve grid-connected synchronization and employs voltage outer-loop control to make U_{GFM} follow v_{dref} [22].

The mathematical model of GFM control can be expressed as:

$$\begin{cases} \dfrac{\mathrm{d}\delta_c}{\mathrm{d}t} = \omega_0\omega_c \\ J\dfrac{\mathrm{d}\omega_c}{\mathrm{d}t} = \dfrac{P_{sref} - P_s}{\omega_c} - D_\delta(\omega_c - \omega_0) \\ \dfrac{\mathrm{d}E_c}{\mathrm{d}t} = K_q(Q_{sref} - Q_s) + K_u(U_{ref} - U_{VSC}) \end{cases} \tag{2}$$

where U_{VSC} and U_{ref} are the voltage amplitude and reference value at the grid-connected node, respectively; K_q is the reactive power coefficient; K_u is the voltage sag coefficient; D_δ is the damping coefficient; E_c is the equivalent electromotive force of GFM-VSC; ω_0 and ω_c are the rated speed and per unit value of actual speed, respectively; δ_c is the equivalent phase angle of GFM-VSC; and J is the inertia factor of GFM-VSC.

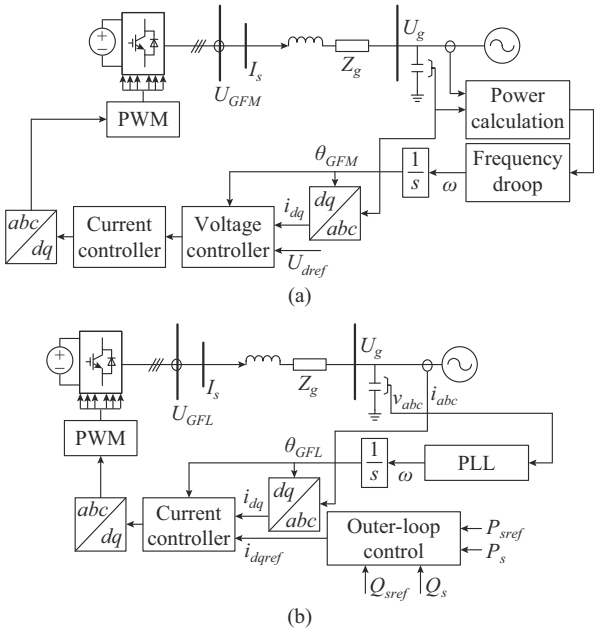

Fig. 1. Framework and structure of GFL-VSC and GFM-VSC. (a) GFL-VSC. (b) GFM-VSC.

Taking the grid-connected voltage of the grid as a reference and ignoring the power loss caused by the filter capacitance of the converter, we can obtain:

$$\begin{cases} P_s = P_{AC} = \dfrac{3}{2}\dfrac{U_g E}{X_L + X_F}\sin\theta \\ Q_s = Q_{AC} = \dfrac{3}{2}\dfrac{E}{X_L + X_F}(E - U_g\cos\theta) \end{cases} \tag{3}$$

where X_L and X_F are the equivalent impedances of the line and VSC, respectively; E and θ are the equivalent electromotive force and phase angle of the converter, respectively; P_{AC} is the active power of the AC line; and Q_{AC} is the reactive power of the AC line.

Based on (3), GFM-VSC can utilize the power synchronization. The amplitude and phase of electromotive force are shaped independently to achieve grid synchronization. Thus, the control-level characteristics differ from those of GFL-VSC.

B. Quantitative Calculation of GFL and GFM Grid-connected Variables Based on Phasor Method

According to the equivalent circuit, if the current command does not reach the inner-loop current limit value [23], we can apply:

$$\begin{cases} I_s = I_{s,ref} = (E - U_g)/(Z + Z_g) \\ U_{VSC} = U_g + Z_g I_s \end{cases} \tag{4}$$

where $I_{s,ref}$ is the reference value of I_s; and Z is the equivalent impedance of the external ports of GFL-VSC and GFM-VSC.

The direction of U_g is aligned with the *x*-axis, forming the phasor space of the voltage. The direction perpendicular to the *x*-axis establishes the *y*-axis. The coordinates of the endpoint of U_{VSC} are (x_U, y_U). The amplitude can be obtained as

$U_{VSC}=\sqrt{x_U^2+y_U^2}$. $\delta=\theta-\theta_g$ is the angle between E and U_g, which is the power angle of the converter.

The contour of the constant voltage control (CVC) curve formed by U_{VSC} is a CVC circle centered at the origin with a radius equal to the amplitude of U_{VSC} [24]. Therefore, if the converter is controlled under constant voltage, the endpoint of U_{VSC} will remain on the contour of the CVC circle. *Q-U* circle characterizes the reactive power and voltage of GFL-VSC and GFM-VSC, which is a collective term for reactive power and voltage curves in the following analysis. Thus, the expression for reactive power can be derived from the *Q-U* circle as:

$$Q_s=\frac{U_{VSC}^2}{X_g}-\frac{U_{VSC}U_g\cos\delta_U}{X_g}\rightarrow\left(x_U-\frac{U_g^2}{2}\right)+y_U^2=X_gQ_s+\frac{U_g^2}{4} \tag{5}$$

where $\delta_U=\theta_U-\theta_g$ is the angle between U_{VSC} and U_g, which determines the location of the endpoint of the converter voltage; and $U_{VSC}\cos\delta_U=x_U$ is derived from the phasor diagram.

The reactive power contour curve is a circle centered at the midpoint of the grid voltage, with a radius of $\sqrt{X_gQ_s+U_g^2/4}$. If constant reactive power control is used, the endpoint of the grid connection will remain on the reactive power contour, satisfying $Q_s=Q_{sref}$.

The expression for the active power at the grid-connected point, calculated from the *Q-U* circle, is given by:

$$P_s=\frac{U_{VSC}U_g\sin\delta_U}{X_g}=\frac{U_gy_U}{X_g}\rightarrow y_U=\frac{P_sX_g}{U_g} \tag{6}$$

The equivalent active power curve is different from the equivalent reactive power curve. When U_g and X_g maintain constant values, the equivalent active power curve of the grid point is a straight line perpendicular to the *y*-axis, resulting in $P_s=P_{sref}$. The vertical coordinates of the endpoint of U_{VSC} can be calculated as $y_U=P_{sref}X_g/U_g$.

Considering that the time scale of the reactive voltage control is much faster than the power angle swing, the endpoint of U_{VSC} will quickly move to and remain on the reactive voltage characteristic curve, while the active power control will adjust the magnitude of the power angle continuously.

In practical engineering, current limiters must be used. Therefore, the current limiter will have an impact on the control dynamics of the converter. In this process, the current limiter acts as a *dq*-axis equalizer, as shown in (7).

$$i_{dqref}=\min\{1,I_{lim}/\|i_{sdqN}\|\}i_{sdqN} \tag{7}$$

where I_{lim} is the current limit value; i_{sdqN} is the magnitude of the *dq*-axis output current of the turbine; and $\|\cdot\|$ represents the magnitude of the *dq*-axis current.

The current limiter is actually a variable gain for the controller under operation. When the amplitude of the current command value is less than the maximum current amplitude, the corresponding limit coefficient is 1. When the amplitude of the current command is greater than the maximum current amplitude, it reduces the amplitude of the current command by a factor of $I_{lim}/\|i_{sdqN}\|$ so that the amplitude of the current reference value will eventually be equal to I_{lim}.

With the phasor equivalence of GFL and GFM controls, the control characteristics can be related to the phasor constraints and trajectory circles, and a quantitative expression of the active and reactive power outputs at the converter ports can be realized.

III. GFL and GFM Dynamic Phasor Model Combined with Topological Homology Method

Topological homology means that two functions are topologically equivalent. One can be obtained from the other by successive topological changes. Since both L_1 and L_2 are circular, the homology relation is satisfied. This means that any control corresponding to a mapping is homomorphic to itself, and if two controls corresponding to the mappings are homomorphic to each other, the control properties between them are also homomorphic in phasor space.

A continuous map *f*, *g* from a topological space *X* to a topological space *y* is homomorphic if *f* can be continuously deformed into *g* in *y*. Suppose *f*, *g*: $X\rightarrow Y$ are continuous mappings, and $I=[0,1]$. If there exists a continuous mapping function H: $X\times I\rightarrow Y$ for all $x\in X$, we can obtain:

$$H(x,0)=f(x),H(x,1)=g(x) \tag{8}$$

When the converter adopts reactive power-voltage sag control, the state coefficient of reactive voltage sag $H(x,y,K_{qu})$ is 0, as shown in (9).

$$H(x,y,K_{qu})=\frac{1}{1-\frac{1}{K_{qu}}}(Q_{sref}-Q_s)+\frac{1}{1-K_{qu}}(U_{ref}-U_{VSC})=\frac{K_q}{K_q+K_u}(Q_{sref}-Q_s)+\frac{K_u}{K_q+K_u}(U_{ref}-U_{VSC}) \tag{9}$$

where K_{qu} is the reactive power-voltage proportionality factor.

According to the phasor diagram, it can be obtained that the reactive power-voltage satisfies the following relationship at steady state: $K_q(Q_{sref}-Q_s)+K_u(U_{ref}-U_s)=0$. Among them, $K_q=0$ corresponds to constant voltage amplitude control; $K_u=0$ corresponds to CQC; and $K_q\neq0$ and $K_u\neq0$ correspond to reactive power sag control. At this time, K_{qu} is calculated as:

$$K_{qu}=\frac{\Delta Q}{\Delta U}=-\frac{K_u}{K_q} \tag{10}$$

where ΔQ is the reactive power variation; and ΔU is the voltage variation.

Therefore, $H(x,y,K_{qu})$ for constant reactive power control is set to be 0 in the I-function, which corresponds to $K_u=0$ and is defined as the open set *R*. The corresponding $H(x,y,K_{qu})$ for constant AC voltage control is set to be 1 in the I-function, which corresponds to $K_q=0$ and is defined as the open set *V*. Therefore, the topology of control mapping in the phasor space of GFM-VSC and GFL-VSC can be decomposed into a concatenation of the two open sets mentioned above. Thereby, the curvilinear relations and trajectories of dynamic process changes in the phasor topological space can be computed from the fundamental groups of *R*

and V, as well as their intersection groups. The mathematical expressions can be given as:

$$\pi_1(X,x,H(x,y,K_{qu}))\cong\frac{\pi_1(R,x_0,H(x,y,1))\pi_1(V,x_0,H(x,y,0))}{N} \tag{11}$$

where N is the regular subgroup generated by all elements of R and V; and π_1 is the topology after control mapping in the phasor space.

Therefore, based on topological homology and phasor spaces, it is possible to transform controls into the topology of the phasor space. This method relates the control properties to the topological trajectories, by which the nature of the continuous transformation between the controls is explained. Furthermore, the topological trajectories reveal the difference between the frequency-voltage control of GFL-VSC and GFM-VSC. The transformations and interrelationships of GFL and GFM controls based on topological homology are shown in Fig. 2, where EC_{max} and EC_{min} are the electromotive force circles when the electromotive force amplitude values are E_{max} and E_{min}, respectively; and C_{GFL} and C_{GFM} are the endpoints of the grid-connected voltage of GFL-VSC and GFM-VSC, respectively.

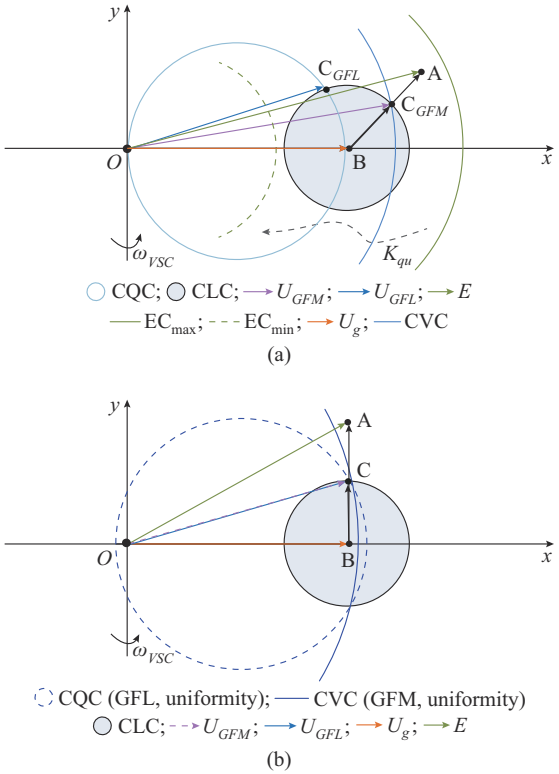

Fig. 2. Transformations and interrelationships of GFL and GFM controls based on topological homology. (a) Phase representation and declaration of each control of GFL-VSC and GFM-VSC. (b) Uniformity of grid-connected GFL-VSC and GFM-VSC.

GFL and GFM controls are mapped into the phasor space. The relative positional relationships between the phasors corresponding to each variable in the circuit are depicted in the phasor space. Subsequent analyses will be based on the dynamics of the process based on the phasor space. Therefore, before proceeding with the analysis, the important curvilinear relationships and coordinate points in the diagram are described in detail as follows:

1) CVC represents the constant magnitude of the line connecting the endpoints of the phasor with the origin of the coordinates.

2) CQC represents the characteristics of GFL-controlled constant power source, which is a circle with half of U_g as the radius and the midpoint of U_g as the center.

3) EC represents the constant electric potential circle, which is a special circle for GFM-VSC and represents electric potential constraint. When voltage changes, this electric potential circle works to ensure that GFM-VSC maintains voltage stability in cases of low voltage and high voltage.

4) CLC represents the current inner-loop circle of the converter. The length of the output current phasor needs to be less than the radius of the inner-loop current limit circle during operation.

In Fig. 2, point A represents the endpoint of the equivalent electromotive force of GFL-VSC and GFM-VSC; point B represents the endpoint of the bus voltage of the grid; and point C represents the endpoint of the grid-connected voltage of GFL-VSC and GFM-VSC. The method proposed in this paper consists of three core steps, which are unfolded in the order shown in Fig. SA2 of Supplementary Material A.

As shown in Fig. 2(a), the Q-U curves of GFL-VSC and GFM-VSC satisfy the topological homology. Homology means that two functions are topologically equivalent, which implies that one can be obtained from the other through successive topological changes. Since both CVC and CQC are circular, the homology relation is satisfied. As shown in Fig. 2(b), since CVC and CQC satisfy the topological homology relation, when K_{qu} increases from 0 to positive infinity, the corresponding curve will change continuously from CVC to CQC. Therefore, different K_{qu} values can characterize the reactive voltage sag control from various perspectives of the topological homology relation. In this case, the internal electric potential of the converter is also constrained by E_{max} and E_{min}. They form an electric potential circle centered at the origin with E_{max} and E_{min} as radii, respectively. Similarly, the output current amplitude of the converter is also limited by I_{lim}, which constitutes a circle centered at the endpoint of U_g with $I_{lim}Z_g$ as the radius. Under low voltage, the active power will be increased by adjusting $Q_{ref,GFL}$, but as the reactive power output further increases, the active power decreases along the trajectory, as shown in (12).

$$Q_{ref,GFL}=-\frac{K_u}{K_q}(U_{ref}-U_s)=-K_{qu}(U_{ref}-U_s) \tag{12}$$

The grid-connected active power and reactive power support characteristics similar to GFM-VSC can be realized by changing the $Q_{ref,GFL}$ value, which reflects the uniformity of GFL-VSC and GFM-VSC. However, under low voltage, the E-U double-loop constraint of GFM-VSC possesses better P_s-Q_s characteristics compared with that of GFL-VSC, which reflects their difference.

IV. Analysis of Frequency-voltage Uniformity and Difference for GFL-VSC and GFM-VSC

A. Frequency and Voltage Dynamic Processes of GFL-VSC and GFM-VSC Based on Phasor Method

The dynamics in this paper refer to the evolution and movement trends of the frequency and voltage of the converter at various moments. Based on the aforementioned analyses, the characteristics of GFL-VSC and GFM-VSC during different frequency-voltage dynamics are summarized and defined as the uniformity and difference of frequency-voltage dynamics. Frequency-voltage dynamic uniformity and difference refer to the uniform and different characteristics of GFL and GFM controls throughout the process of active power-frequency and reactive power-voltage changes after the frequency and voltage changes. The dynamics involve four moments: the initial operation state, the instant of frequency-voltage change, the sustained phase of frequency-voltage change, and the system reaching a new stable state.

The dynamic process of frequency-voltage includes the synchronization process of the converter and the dynamic process of control. The synchronization process affects the synchronization stability of the converter, which has an important influence on the dynamic process of GFL-VSC and GFM-VSC under frequency-voltage changes. In addition, on the basis of ensuring synchronization, the dynamic process of control determines the equivalent external characteristics of the frequency-voltage change of the converter.

As shown in Fig. 3(a), the synchronization process of GFL-VSC and GFM-VSC is to track the voltage or current component. The angles which are relative to the *xy* frame are obtained as the output angles. U_{g0} and δ_{v0} are the amplitude and phase of the steady-state grid voltage, respectively. At the instant of voltage change, U_{gF} and δ_{vF} are the amplitude and phase of the transient-state grid voltage, respectively. $\angle\delta_{PLL}$ is the PLL output phase angle of GFL-VSC. As shown in Fig. 3(b), I_{c0} and δ_{i0} are the amplitude and phase of the steady-state grid current, respectively. At the instant of voltage change, I_{gF} and δ_{iF} are the amplitude and phase of the transient-state grid current, respectively. $\angle\delta_{GFM}$ is the phase angle of GFM-VSC. The synchronization of GFL-VSC and GFM-VSC differs in voltage source and current source. The control objective of PLL for GFL-VSC is to estimate the phase angle of the grid voltage.

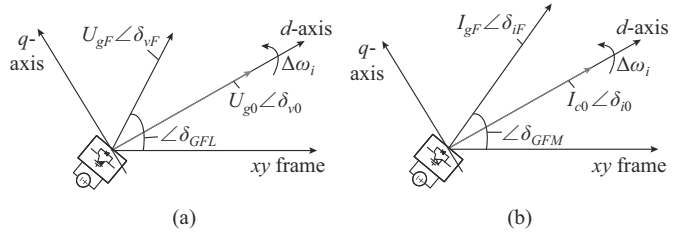

Fig. 3. Synchronization process and difference for GFL-VSC and GFM-VSC. (a) GFL-VSC. (b) GFM-VSC.

The voltage phase angle of GFL-VSC is measured by controlling U_q to 0. U_q is also proportional to Q_s. For GFM-VSC, P_s-ω sag is equivalent to i_d-ω sag. GFM-VSC follows i_d or P_s: $i_d \propto P_s = U_d i_d + U_q i_q = U_d i_d$. The change in P_s is directly proportional to that in i_d when GFM control maintains U_d constant with the voltage outer loop. While GFL-VSC follows U_q or Q_s: the change in Q_s is directly proportional to that in U_q when GFL-VSC maintains i_d constant with the current outer loop. $U_q \propto Q_s = U_q i_d - U_d i_q = U_q i_d$, forming a voltage-current duality synchronization. GFM-VSC has current angle swing characteristics, while GFL-VSC has voltage angle swing characteristics. However, the synchronization of GFM-VSC is not dependent on the operation of U_g due to CLC, but is affected by the P_s-i_d upper limit, resulting in reaching synchronization saturation. While GFL-VSC has a synchronization process that is directly affected by the grid-connected voltage but can be followed continuously due to its synchronization process when ensuring $U_q = 0$.

Based on the above circuit relationships, constraints, and quantitative calculations, the control dynamics of active power-frequency and reactive power-voltage of GFL-VSC and GFM-VSC are portrayed using the phasor method, and the dynamic characteristics of frequency and voltage are analyzed. The difference between GFL-VSC and GFM-VSC at the transient instant is shown in Fig. SA3 of Supplementary Material A.

As shown in Fig. 4(a), GFL-VSC makes U_{GFL} move along the CQC. The trajectory of CQC moves to the left as U_g decreases. The trajectory of CLC is gradually increased to the limit along with U_g. Since the radius of the CQC changes with U_{GFL}, GFL-VSC responds passively to the voltage change. As shown in Fig. 4(b), GFM-VSC employs active frequency control under ω_{VSC} acceleration, thus θ increases. The voltage outer-loop control regulates GFM-VSC to move along the CVC to keep U_{GFM} constant and supports the voltage at the PCC combined with the active frequency control. CLC of GFM-VSC is the boundary of the current [25]. In Fig. 4, subscript 0 represents the corresponding curve is in the initial state; and subscripts 1 and 2 represent the curves that are in a dynamic process.

The dynamic phasor analyses considering rotation of the *xy* frame are shown in Fig. SA4 of Supplementary Material A. The trajectories of GFL-VSC and GFM-VSC with K_{qu} and Q_{ref} under high and low voltage variations are shown in Fig. SA5, SA6, and SA7 of Supplementary Material A.

As shown in Fig. 5(a), the trajectories of GFL-VSC and GFM-VSC are different. The topological trajectory of GFL-VSC rotates relatively with the rotation of the grid-connected voltage, which is a clockwise direction during the frequency drop. Each of the three states forms a corresponding phasor triangle and an angular difference from the original reference axis. During active frequency support, the radius of the output current circle further increases due to the increase in active power output. There exists a control-caused trajectory variability, in which the trajectories of both can be computed from the phasor constraint relationship. Similarly, controlled by the CVC, the topological trajectory of GFM-VSC rotates clockwise with the trajectory of the CVC. In this process, GFM-VSC can ensure that the port voltage remains constant. Additionally, the radius of the CLC increases equally with the active power output.

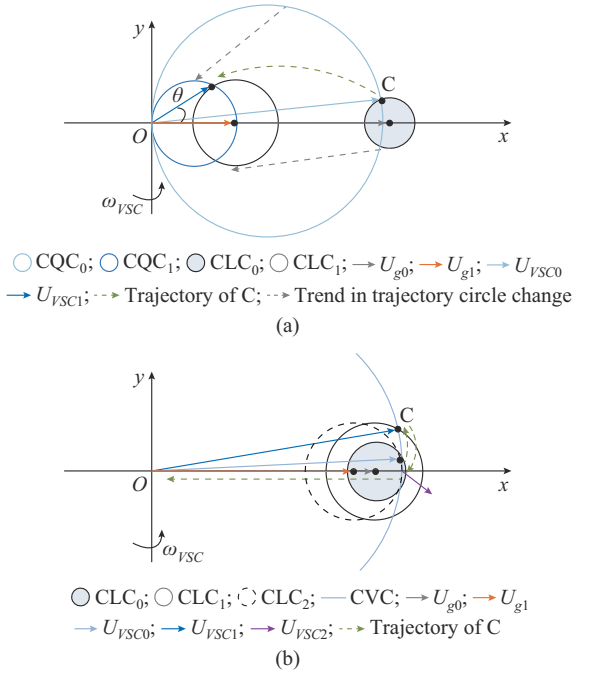

Fig. 4. Voltage drop response of GFL-VSC and GFM-VSC. (a) GFL-VSC. (b) GFM-VSC.

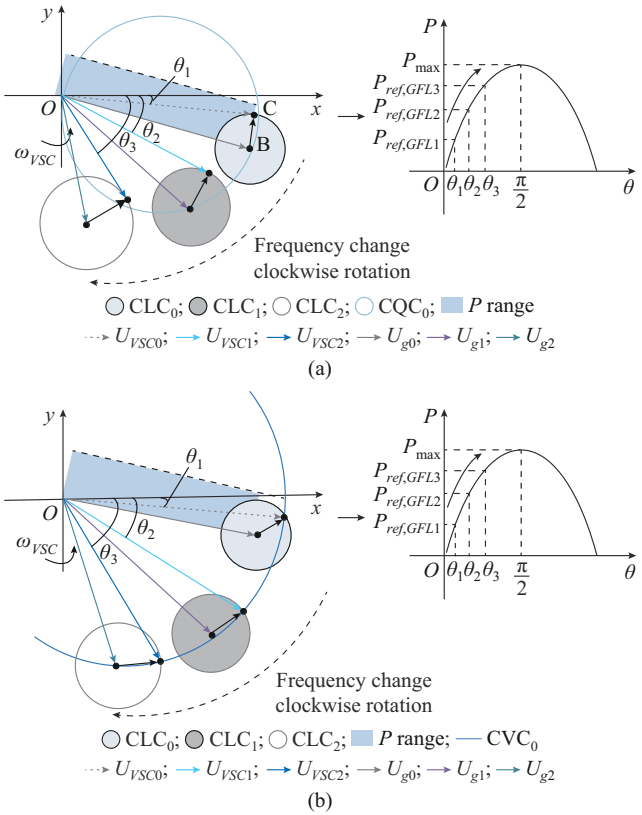

Fig. 5. Frequency drop response of GFL-VSC and GFM-VSC. (a) GFL-VSC. (b) GFM-VSC.

As shown in Fig. 5(b), the phase speed of GFM-VSC and GFL-VSC drops from ω_0 to ω_{VSC}. Since the electromotive force of GFM-VSC cannot change instantaneously and abruptly, the voltage moves counterclockwise along the voltage circle. The grid-connected voltage of GFL-VSC mutates along the CQC, changing from U_{VSC0} to U_{VSC2}. The reference value of the active power for GFL-VSC gradually changes from $P_{ref,GFL1}$ to $P_{ref,GFL3}$. However, the reference value is not allowed to exceed P_{max} to avoid system instability. GFM-VSC employs active frequency control to accelerate ω_{VSC}, and thus θ increases. The active power output increases to support the frequency [26], which further contributes to the difference in frequency regulation dynamics between GFL-VSC and GFM-VSC. GFL-VSC can vary with voltage due to the reactive power circle during frequency regulation. The relative position between the reactive power circle and the CLC can vary up to the highest point of the CLC. Then, the exhaustible active power output can be independent of voltage outer-loop constraints. When U_{VSC} is in a quasi-steady state, GFL-VSC has a steady-state reactive power output of 0 due to the application of CQC. GFM-VSC applies CVC, which requires a reactive power output to support the voltage. Therefore, GFL-VSC has a larger active power output limit in quasi-steady state.

B. Process Analysis of Quasi-steady State of GFM-VSC and GFL-VSC with Action of SCR

The control coupling of GFL-VSC and GFM-VSC is shown in Figs. SA8 and SA9 of Supplementary Material A. The derivation can be obtained according to the phase-volume relationship shown in Fig. 6(a). It can be observed that the coupling component of the active power generated by GFM voltage regulation increases subsequently. The magnitude of this coupling component is indicated by the length of the purple double-arrow curve.

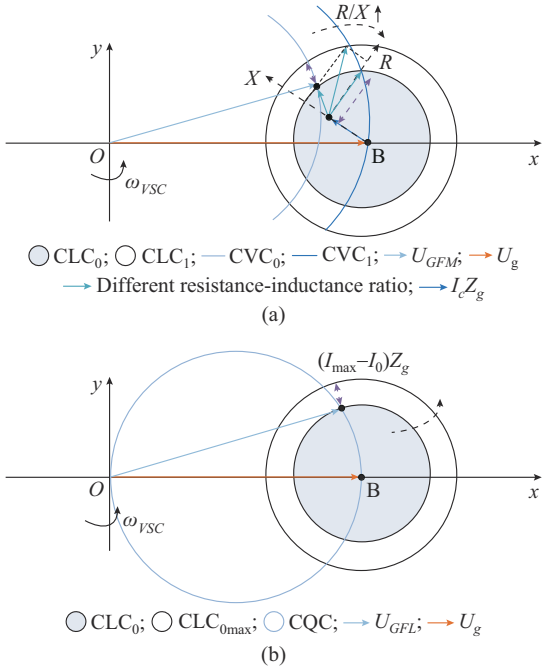

Fig. 6. Control coupling of GFM-VSC and GFL-VSC. (a) Relationship between degree of GFM-VSC coupling and resistance-inductance ratio. (b) Relationship between degree of GFL-VSC coupling and change of impedance.

As shown in Fig. 6(b), the grid-connected impedance Z_g of GFL-VSC varies from Z_{g1} to Z_{g2}. The increase of the grid-

connected impedance corresponds to that of the radius of the CLC. At this time, the corresponding grid-connected voltage varies from U_1 to U_2, which decreases with the increase of Z_g. As the active support of GFL-VSC is activated, its coupling will be proportional to the magnitude of the impedance. Therefore, when the impedance becomes large, the amount of coupling will increase, and the coupling amount of GFL-VSC is proportional to the impedance magnitude, as shown in (13).

$$\Delta P_{s\max}/Q_{s\max}=(I_{lim}^2-I_0^2)Z_g \tag{13}$$

where $\Delta P_{s\max}$ and $Q_{s\max}$ are the maximum active power and reactive power coupling quantities, respectively.

C. Boundary Analysis of GFM-VSC and GFL-VSC in Full-condition Operation

The feasible domain of frequency-voltage operation represents the active power-frequency support capability of GFL-VSC and GFM-VSC in different voltage operation states. This feasible operation interval can be portrayed by *xy* equivalent area in the phasor space, where the *x*-axis is related to the grid-connected voltage, and *y*-axis is related to the real-time active power output.

The operation ranges of GFL-VSC and GFM-VSC are indicated under the variation of U_g in Fig. SA10 of Supplementary Material A. As shown in Fig. SA10, GFL-VSC initiates the high-/low-voltage ride-through control when the voltage is lower than 0.9 p.u. or higher than 1.1 p.u.. Therefore, the operation range of 0.9-1.1 p.u. is the overlapping range between GFM-VSC and GFL-VSC. In the interval below 0.9 p.u., GFM-VSC can support the grid voltage through *E*-*U* double-loop control and can change with *E*-θ to realize the full coverage of the operation range below 0.9 p.u.. In addition, GFL-VSC can realize the same frequency-voltage control effect by adjusting Q_{ref}. However, when the CLC and the reactive power circle radius are the same, we can obtain:

$$y_{U,GFL}=\sqrt{\frac{3U_g^2}{16}-\left(\frac{X_gQ_s}{U_g}\right)^2}+\frac{X_gQ_s}{2} \tag{14}$$

where $y_{U,GFL}$ is the trajectory of the *y*-axis of GFL-VSC.

The above state represents the cut-off point in the middle of the voltage drop process. When the voltage drops again, if Q_{ref} is not increased, the value of *y* at the intersection of GFL-VSC will drop to 0, as shown in (15). Similarly, when the voltage is higher than 1.1 p.u., GFM-VSC and GFL-VSC have a uniform operation interval. The difference is that when U_g is within 0.9-1.1 p.u., GFM-VSC can realize the operation interval coverage in the range of 0.9-1.1 p.u., as shown in (16).

$$S_{GFL}=\int_0^{0.9}X_gI_{lim}\mathrm{d}x+\int_{0.9}^{1.1}\sqrt{(X_gI_c)^2-\left(-\frac{(X_gI_c)^2}{U_g}+\frac{X_gQ_s}{U_g}\right)^2}\,\mathrm{d}x+\int_{1.1}^{U_g}X_gI_{lim}\mathrm{d}x \tag{15}$$

$$S_{GFM}=\int_0^{U_g}X_gI_{lim}\mathrm{d}x \tag{16}$$

where S_{GFL} denotes the area of the feasible domain enclosed by GFL-VSC in the phasor space; and S_{GFM} denotes the area of the feasible domain enclosed by GFM-VSC in the phasor space.

It is precisely due to the upper limit of quasi-steady-state active power for grid-connected voltage in the range of 0.9-1.1 p.u.. Further analyses of the causes reveal the operation trajectory of GFL-VSC, whose voltage phasor moves to the lower left as the voltage decreases.

The *y*-value at the intersection of reactive power and CLC will gradually decrease. This, in turn, causes the difference in the operation intervals between them, which reflects the difference between active and passive regulation of GFL-VSC and GFM-VSC in the quasi-steady state.

V. Case Study

In order to verify the effectiveness of the proposed method in revealing the frequency-voltage uniformity and difference between GFM-VSC and GFL-VSC, GFL-VSC and GFM-VSC are integrated into a four-machine two-area system, which is constructed on the MATLAB/Simulink platform, as shown in Fig. 7. The models involve multiple GFL-VSC units and GFM-VSC units. Each unit represents an aggregated model of renewable energy generation with different capacities. The capacity of each GFM-VSC unit is 80 MW, and the capacity of each GFL-VSC unit is 50 MW. The base capacity of the system is 100 MVA.

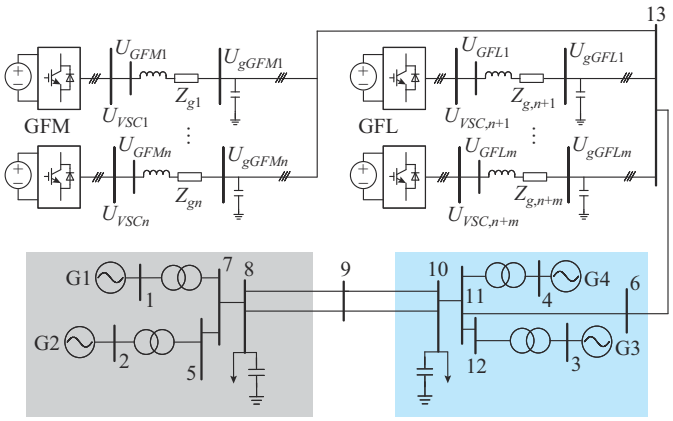

Fig. 7. GFL-VSC and GFM-VSC integrated into four-machine two-area system.

A. Simulation Verification Analysis of Frequency-voltage Dynamic Processes of GFM-VSC and GFL-VSC

As shown in Fig. 8(a) and (b), when a severe voltage drop in U_g occurs, the U_{VSC} of GFM-VSC is better than that of GFL-VSC due to the voltage-supporting control of GFM-VSC. Consequently, under low-voltage conditions, the active power output of GFL-VSC is lower compared with that of GFM-VSC. The voltage versus active power relationship is satisfied when $P_{\max}=E_{lim}I_{lim}$. In addition, when GFL-VSC satisfies this relationship under low-voltage conditions, the port voltages of GFL-VSC and GFM-VSC form a similar effect to the active power output, which reflects their uniformity. Note that in Fig. 8, U_{GFLCd} is the *d*-axis component of the

GFL-VSC grid-connected voltage under the control of changing $Q_{ref,GFL}$; U_{GFLd} and U_{GFMd} are the d-axis components of the grid-connected voltage of GFL-VSC and GFM-VSC, respectively; P_{GFLC} is the active power of GFL-VSC under the control of changing $Q_{ref,GFL}$; P_{GFL} and P_{GFM} are the active power of the GFL-VSC and GFM-VSC, respectively.

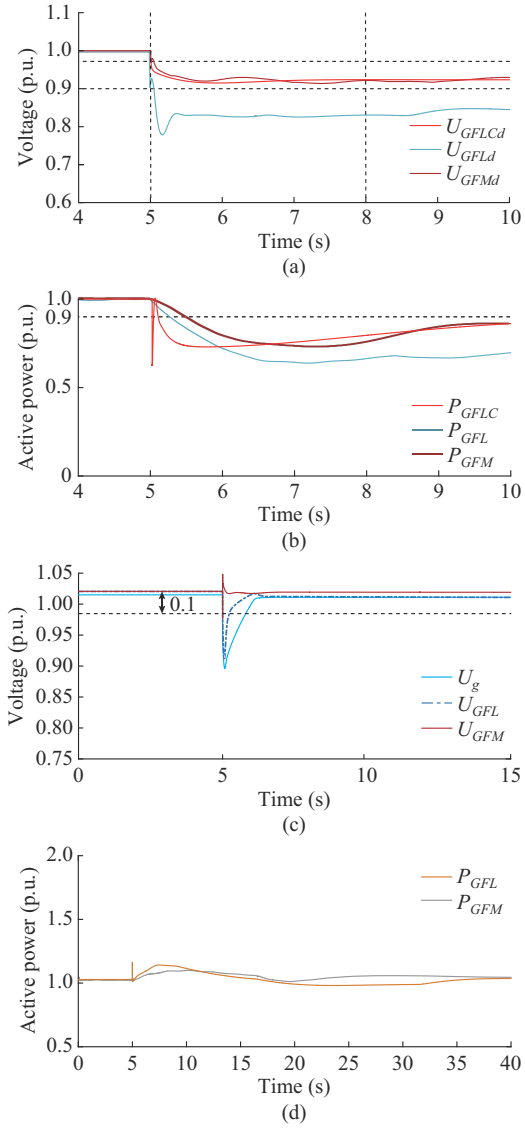

Fig. 8. Simulation verification analysis of frequency-voltage dynamic processes of GFM-VSC and GFL-VSC. (a) Severe voltage drop of GFM-VSC and GFL-VSC. (b) Active power output of GFM-VSC and GFL-VSC under severe voltage drop. (c) Voltage of GFM-VSC, GFL-VSC, and grid. (d) Active power output of GFM-VSC and GFL-VSC.

As shown in Fig. 8(c) and (d), when U_g drops to 0.9 p.u., the voltage of GFM-VSC recovers after a sudden change. The voltage of GFL-VSC drops to 0.92 p.u., and active power output of GFM-VSC varies less due to voltage stabilization. Meanwhile, GFL-VSC keeps the reactive power output as 0, thus the short-term active power output can increase to 1.1 p.u..

As shown in Fig. SA11 of Supplementary Material A, the quantitative relationship between voltage change and active power is also verified.

B. Validation of Uniformity and Difference in Frequency and Voltage Dynamics of GFL-VSC and GFM-VSC

As shown in Fig. SA12 of Supplementary Material A, the dynamic processes and response characteristics of active power and voltage are verified. As shown in Fig. 9(a) and (c), GFL-/GFM-VSC station contains 15 GFL-VSCs and 5 GFM-VSCs. The active power output variation of GFL-VSCs is larger than that of GFM-VSCs when an active power surplus occurs, resulting in a frequency increase, and the active power output variations of GFL-VSCs gradually converge. The active power output variations of GFM-VSCs follow respective Q-U curves, and the trajectories do not overlap. The dynamic response processes are different. When there is an active power surplus and no reactive power deficit, U_g remains stable in the steady state at this time.

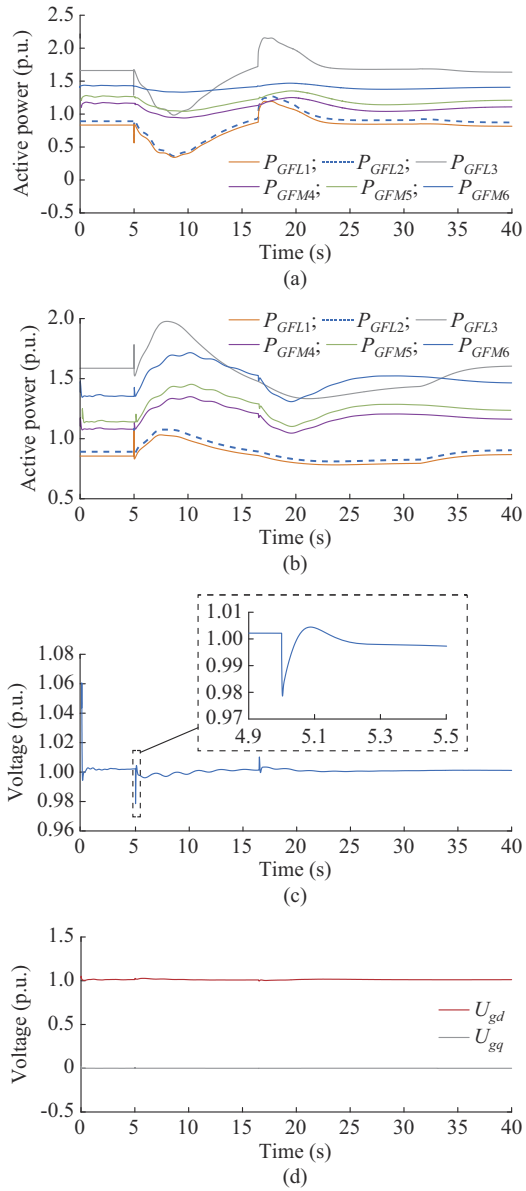

Fig. 9. Simulation and verification analysis of multi-machine grid-connected dynamic processes in GFL-/GFM-VSC station. (a) Active power output of GFL-VSC and GFM-VSC under voltage drop. (b) Active power output of GFL-VSC and GFM-VSC under frequency drop. (c) Voltage of U_g under voltage drop. (d) Voltage of U_g under frequency drop.

As shown in Fig. 9(b) and (d), when a frequency drop occurs, U_g of GFL-VSC and GFM-VSC that constitute the station will drop slightly with the movement of the *Q-U* curve. The results of the active power exhaustion output show that GFL-VSC has more active power support margins due to the adoption of the CQC in the steady state. In contrast, because GFM-VSC provides reactive power output in the steady state to support the voltage, its output has a smaller active power margin compared with GFL-VSC.

C. Operation Interval of GFL-VSC and GFM-VSC in Multi-case Quasi-steady State

As shown in Fig. SA13 of Supplementary Material A, the effects of K_{qu} variation in GFM-VSC and reactive power output variation in GFL-VSC are compared.

In Fig. 10(a), using the *Q-U* curve as the boundary line, the destabilization region and the destabilization point of the voltage can be judged.

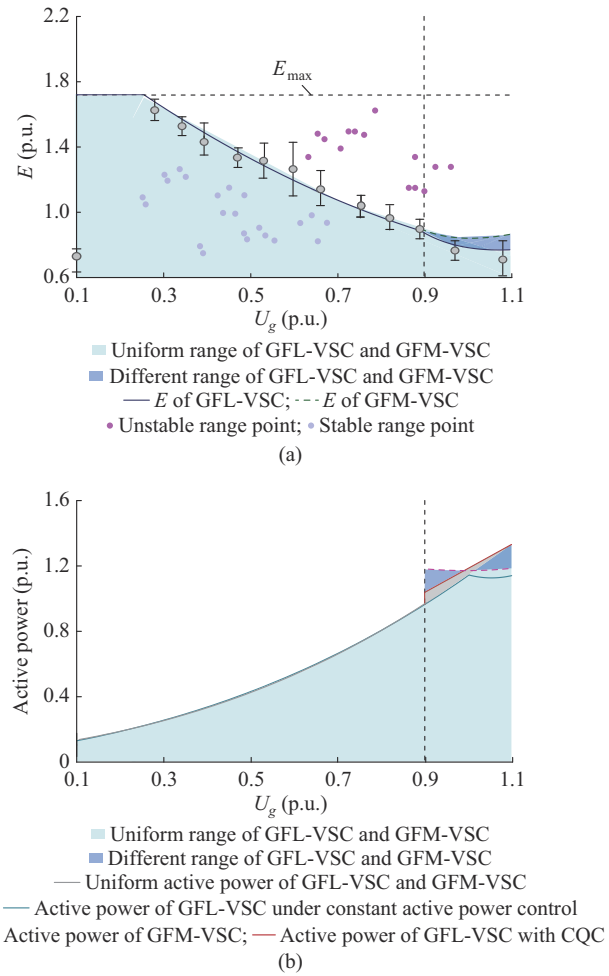

Fig. 10. Validation of operation intervals of GFL-VSC and GFM-VSC in quasi-steady state with multiple operation conditions. (a) Uniform and different range between electromotive force and voltage of GFL-VSC and GFM-VSC. (b) Uniform and different range between active power and voltage of GFL-VSC and GFM-VSC.

As shown in Fig. 10(b), the difference between the uniform and different ranges of GFL-VSC and GFM-VSC lies in the voltage source control of GFM-VSC, which leads to the grid-connected voltage constraint. The active power output remains near 1.2 p.u., satisfying the maximum current inner-loop constraint. Because of the control characteristics of the current source, GFL-VSC shows an approximately linear output relationship with the grid-connected voltage while satisfying the maximum current inner-loop constraint. This reflects the difference between GFL-VSC and GFM-VSC in the voltage interval of 0.9-1.1 p.u..

According to Fig. 10, GFM-VSC can operate in the maximum voltage of 1.1 p.u. due to the adjustable CVC and K_{qu}. The *y*-axis imposes limitations of $E_{\min}$ and $E_{\max}$ on the operation state. The *Q-U* curve of GFL-VSC is obtained from the CQC of GFL-VSC. When K_{qu} of GFM-VSC is set to be 1, both GFM-VSC and GFL-VSC share the same *Q-U* control as well as identical voltage interval ranges, and exhibit uniformity in their performance. In the operational domain, the difference between GFL-VSC and GFM-VSC lies in the range of U_g from 0.9 to 1.1 p.u.. When GFL-VSC is controlled with constant reactive power as 0, the output boundary of the active power is limited by the upper limit of the current inner loop. The active power increases as the voltage within the range of U_g varies from 0.9 to 1.1 p.u.. The active power output remains constant under constant active power control. The active power of GFM-VSC maintains a constant value in the range of U_g from 0.9 to 1.1 p.u., and the upper limit of active output is determined by the current inner loop. This also highlights the difference between GFL-VSC and GFM-VSC.

D. Summary on Frequency-voltage Uniformity and Difference Dynamics Between GFM-VSC and GFL-VSC

The conclusions on the evolution and movement trends of the frequency-voltage at various dynamic moments are further summarized as the uniformity and difference in the dynamics of GFL-VSC and GFM-VSC.

In terms of the difference in the dynamic process: when $K_{qu} \neq 1$, GFM-VSC has better weak-grid operation capability, while GFL-VSC has better strong-grid operation capability. GFM-VSC has independent synchronization with current-following current angle swing, but it is affected by the P-i_d limit, resulting in synchronization saturation. GFL-VSC has a voltage-following voltage angle swing characteristic and exhibits current-source dynamics. At the transient instant, the transient output current of GFL-VSC remains constant, while GFM-VSC keeps the transient electromotive force and voltage constant. The control couplings of GFL-VSC and GFM-VSC are different. The control coupling of GFM-VSC is from virtual synchronous control and voltage control. However, the control coupling of GFL-VSC is from the phase angle of a PLL. Additionally, in the aspect of converter-grid coupling, GFM-VSC coupling is proportional to line inductive reactance, while GFL-VSC coupling is proportional to grid-side impedance. GFL-VSC has active-power-to-reactive-power and reactive-power-to-active-power couplings in the power regulation process in weak grid, while GFM-VSC has only reactive-power-to-active-power coupling. In the dynamic voltage support process, GFM-VSC has better voltage support and can establish voltage independently. The

voltage adjustment of GFL-VSC is passive. In the dynamic frequency adjustment process, GFL-VSC has a wider active support margin due to $Q_{ref0}=0$ in the steady state, but its active output capability is weaker than that of GFM-VSC under low voltage. The upper limit of quasi-steady-state active power for grid-connected voltage of GFM-VSC in the range of 0.9 p.u. to 1.1 p.u. is larger.

GFL-VSC is also uniform with GFM-VSC. When $K_{qu}=1$ for GFM-VSC, GFM-VSC and GFL-VSC possess the uniformity of the Q-U curve. Or when $Q_{ref,GFL}=-(K_u/K_q)(U_{ref}-U_s)=-K_{qu}(U_{ref}-U_s)$ is satisfied, the grid-connected operation points of both are the same, and the feasible domains overlap completely. The basis of this stems from the uniformity of the Q-U curves, so that there will be similar voltage and frequency support effects. In addition, the reactive power to active power coupling effect is present in both control couplings. Also, both types of control coupling and converter-grid coupling exist. Table SAI of Supplementary Material A compares the applicability of various research methods. Table SAII summarizes the uniformity and difference between GFL-VSC and GFM-VSC.

VI. Conclusion

In this paper, a dynamic analysis of the uniformity and difference for GFL-VSC and GFM-VSC using phasor and topological homology methods is proposed. It is revealed that the voltage and active power linearly correspond to the horizontal and vertical axes in the phasor space referenced to the grid voltage phasor. Thus, the operation point is endowed with the characteristic information of frequency and voltage simultaneously. The topological homology of control curves is the essential source of the difference between them. Their uniformity and difference are investigated through theoretical derivation combined with simulation experiments. The frequency-voltage uniformity and difference between GFL-VSC and GFM-VSC are also obtained.

In terms of the difference, GFL-VSC and GFM-VSC differ in synchronization and interface features, frequency and voltage dynamic responses, power coupling mechanisms, and active power upper limits in quasi-steady state for grid-connected voltage in the range of 0.9 p.u. to 1.1 p.u.. In terms of the uniformity, GFL-VSC and GFM-VSC possess uniformity in terms of power response and phasor trajectory when the conditions of uniformity mentioned in this paper are satisfied, which results in similar voltage and frequency supports. In addition, there is an interplay between reactive power and active power in both GFL-VSC and GFM-VSC. This interplay encompasses both types of coupling: control coupling and converter-grid coupling.

The conclusions summarized in this paper can clarify the uniformity and difference in frequency-voltage dynamic characteristics between GFL-VSC and GFM-VSC, which can be widely applied in various aspects of renewable energy systems, such as the optimized planning and development of control strategies during the operation of GFL-VSC and GFM-VSC.

References

[1] M. Ndreko, S. Rberg, and W. Winter, "Grid forming control for stable power systems with up to 100 power electronic interfaced generation: a case study on great britain test system," *IET Renewable Power Generation*, vol. 14, no. 8, pp. 1268-1281, May 2020.

[2] H. Zhao, H. Zhou, W. Yao *et al.*, "Multi-stage sequential network energy control for offshore AC asymmetric fault ride-through of MMC-HVDC system integrated offshore wind farms," *International Journal of Electrical Power & Energy Systems*, vol. 151, p. 109180, Sept. 2023.

[3] H. Zhang, W. Xiang, W. Lin *et al.*, "Grid forming converters in renewable energy sources dominated power grid: control strategy, stability, application, and challenges," *Journal of Modern Power Systems and Clean Energy*, vol. 9, no. 6, pp. 1239-1256, Nov. 2021.

[4] Y. Peng, Y. Li, K. Lee *et al.*, "Coordinated control strategy of PMSG and cascaded H-Bridge STATCOM in dispersed wind farm for suppressing unbalanced grid voltage," *IEEE Transactions on Sustainable Energy*, vol. 12, no. 1, pp. 349-359, Jan. 2021.

[5] S. Wang, Y. Li, M. Zhang *et al.*, "Harmonic resonance suppression with inductive power filtering method: case study of large-scale photovoltaic plant in China," *IEEE Transactions on Power Electronics*, vol. 38, no. 5, pp. 6444-6454, May 2023.

[6] H. Zhou, W. Yao, K. Sun *et al.*, "Dynamic reactive current optimization based onshore AC fault ride-through strategy for MMC-HVDC integrated offshore wind farms," *IEEE Transactions on Sustainable Energy*, vol. 15, no. 2, pp. 735-746, Feb. 2024.

[7] H. Zhou, W. Yao, K. Sun *et al.*, "Enhancing fault ride-through and voltage support capability for MMC-HVDC integrated offshore wind farms using multi-mode matching approach," *IEEE Transactions on Sustainable Energy*, vol. 15, no. 2, pp. 1256-1268, Feb. 2024.

[8] J. Sun, "Two-port characterization and transfer immittances of AC-DC converters–Part I: modeling," *IEEE Open Journal of Power Electronics*, vol. 2, pp. 440-462, Aug. 2021.

[9] J. Sun, "Two-port characterization and transfer immittances of AC-DC converters – Part II: applications," *IEEE Open Journal of Power Electronics*, vol. 2, pp. 483-510, Mar. 2021.

[10] W. Du, F. K. Tuffner, K. P. Schneider *et al.*, "Modeling of grid-forming and grid-following inverters for dynamic simulation of large scale distribution systems," *IEEE Transactions on Power Delivery*, vol. 36, no. 4, pp. 2035-2045, Aug. 2021.

[11] X. Wang, M. G. Taul, H. Wu *et al.*, "Grid-synchronization stability of converter-based resources – an overview," *IEEE Open Journal of Industrial Applications*, vol. 1, pp. 115-134, Aug. 2020.

[12] W. Du, F. Tuffner, K. Schneider *et al.*, "Modeling of grid-forming and grid-following inverters for dynamic simulation of large scale distribution systems," *IEEE Transactions on Power Delivery*, vol. 36, no. 4 pp. 2035-2045, Aug. 2021.

[13] S. Li, M. Cao, X. Lei *et al.*, "Frequency characteristics of power system involving virtual inertia and primary frequency regulation of wind power based on modified SFR model," *Renewable Energy Resources*, vol. 37, no. 5, pp. 694-700, May 2019.

[14] Y. Li, Y. Gu, and T. Green, "Revisiting grid-forming and grid-following inverters: a duality theory," *IEEE Transactions on Power Systems*, vol. 37, no. 6, pp. 4541-4554, Nov. 2022.

[15] X. Fu, J. Sun, M. Huang *et al.*, "Large-signal stability of grid-forming and grid-following controls in voltage source converter: a comparative study," *IEEE Transactions on Power Electronics*, vol. 36, no. 7, pp. 7832-7840, Dec. 2021.

[16] J. Li, Y. Li, Z. Du *et al.*, "Damping turning rule of virtual synchronous generator for global stability," *IEEE Transactions on Power Delivery*, vol. 38, no. 4, pp. 2650-2660, Aug. 2023.

[17] R. Rosso, X. Wang, M. Liserre *et al.*, "Grid-forming converters: control approaches, grid-synchronization, and future trends – a review," *IEEE Open Journal of Industrial Applications*, vol. 2, pp. 93-109, Apr. 2021.

[18] Y. Zhang, C. Zhang, X. Cai *et al.*, "Current-constrained transient voltage response analysis and an improved fault-ride through control of the virtual synchronous generator," *Proceedings of the CSEE*, vol. 44, no. 15, pp. 5996-6009, Aug. 2024.

[19] L. Guan and J. Yao, "Dynamic coupling and cooperative control for multi-paralleled doubly fed induction generator wind farms during symmetrical low voltage ride-through in a weak grid," *Protection and Control of Modern Power Systems*, vol. 9, no. 3, pp. 112-125, May 2024.

[20] M. Zhang, X. Dou, J. Zhao *et al*., "Two-level coupling-based frequency control strategy with adaptive distributed frequency consensus and

dynamic compensation," *Journal of Modern Power Systems and Clean Energy*, vol. 12, no. 6, pp. 1918-1929, Nov. 2024.
[21] X. Wang, "Unified impedance model of grid-connected voltage-source converters," *IEEE Transactions on Power Electronics*, vol. 33, no. 2, pp. 1775-1787, Feb. 2018.
[22] P. Chen, C. Qi, and X. Chen, "Virtual inertia estimation method of DFIG-based wind farm with additional frequency control," *Journal of Modern Power Systems and Clean Energy*, vol. 9, no. 5, pp. 1076-1087, Sept. 2021.
[23] M. G. Taul, X. Wang, P. Davari *et al.*, "Current limiting control with enhanced dynamics of grid-forming converters during fault conditions," *IEEE Journal of Emerging and Selected Topics in Power Electronics*, vol. 8, no. 2, pp. 1062-1073, Jun. 2019.
[24] Q. Shi, G. Wang, and H. Li, "Coordinated virtual inertia control strategy of Professor multiple wind turbines in wind farms considering frequency regulation capability," *Power System Technology*, vol. 43, no. 11, pp. 4005-4017, Nov. 2019.
[25] K. Sun, W. Yao, J. Wen *et al.*, "A two-stage simultaneous control scheme for the transient angle stability of VSG considering current limitation and voltage support," *IEEE Transactions on Power Systems*, vol. 37, no. 3, pp. 2137-2150, May 2022.
[26] V. A. F. Almeida, G. N. Taranto, and J. M. T. Marinho, "Phasor-domain dynamic model of asymmetric current injection controller for converter-interfaced generator," *Journal of Modern Power Systems and Clean Energy*, vol. 9, no. 6, pp. 1269-1278, Nov. 2021.

Haiyu Zhao received the B. S. degree in electrical engineering from the School of Electrical and Electronic Engineering, North China Electric Power University, Beijing, China, in 2022. He is currently working toward the Ph. D. degree in electrical engineering at Huazhong University of Science and Technology, Wuhan, China. His research interests include stability analysis and control of renewable power system.

Hongyu Zhou received the B. S. degree in electrical engineering from Southwest Jiaotong University, Chengdu, China, in 2020. He is currently pursuing the Ph. D. degree in electrical engineering at Huazhong University of Science and Technology, Wuhan, China. His current research interests include stability analysis and control of high-capacity renewable power system and AC/DC hybrid power system.

Wei Yao received the B.S. and Ph.D. degrees in electrical engineering from Huazhong University of Science and Technology (HUST), Wuhan, China, in 2004 and 2010, respectively. He was a Post-doctoral Researcher with the Department of Power Engineering, HUST, from 2010 to 2012 and a Post-doctoral Research Associate with the Department of Electrical Engineering and Electronics, University of Liverpool, Liverpool, UK, from 2012 to 2014. Currently, he has been a Professor with the School of Electrical and Electronics Engineering, HUST. His current research interests include power system stability analysis and control, renewable energy, high-voltage direct current (HVDC) and DC grid, and application of artificial intelligence in smart grid.

Qihang Zong received the B.S. degree in electrical engineering from Hefei University of Technology, Hefei, China, in 2021. Currently, he is pursuing the Ph. D. degree in electrical engineering at Huazhong University of Science and Technology, Wuhan, China. His research interests include transient stability analysis and control of renewable power system.

Jinyu Wen received the B.Eng. and Ph.D. degrees all in electrical engineering from Huazhong University of Science and Technology (HUST), Wuhan, China, in 1992 and 1998, respectively. He was a Visiting Student from 1996 to 1997 and Research Fellow from 2002 to 2003 all at the University of Liverpool, Liverpool, UK, and a Senior Visiting Researcher at the University of Texas at Arlington, Arlington, USA, in 2010. From 1998 to 2002, he was a Director Engineer in XJ Electric Co. Ltd., Xuchang, China. In 2003, he joined the HUST and now is a Professor at HUST. His current research interests include renewable energy integration, energy storage application, DC grid, and power system operation and control.